Journal of Materials Chemistry A

PAPER

View Article Online
View Journal | View Issue

Cite this: J. Mater. Chem. A, 2014, 2, 19095

Inkjet-printed highly conductive transparent patterns with water based Ag-doped graphene†

Lihong Li, Yuzhen Guo, Xingye Zhang and Yanlin Song*

Received 12th August 2014
Accepted 19th September 2014

DOI: 10.1039/c4ta04156a

www.rsc.org/MaterialsA

Inkjet-printing-based fabrication has been a promising approach with the rapid development and deployment of new material inks. Previous studies have demonstrated inkjet printing of reduced graphene oxide (rGO) or pristine graphene flakes produced by the liquid phase exfoliation method for various devices. Nevertheless, it is still a challenge to inkjet-print conductive patterns with a metal and graphene-based hybrid ink, and to explore the structure effect of metal nanoparticles on the conductivity of graphene-based transparent patterns. Herein, we present a holistic approach to achieve high-performance printed Ag nanotriangle platelet–rGO (Ag NTP–rGO) and Ag polyhedral nanoparticle–rGO (Ag NP–rGO) patterns that addresses the entire process starting from graphene oxide exfoliation, ink formation, printing, to final reduction. Central to this approach is that the solvent of inks is only water, monodisperse Ag nanotriangle platelets (Ag NTPs) and Ag polyhedral nanoparticles (Ag NPs) can be self-assembled on GO which is also used as a dispersant and a stabilizer, and after reduction, compared with rGO, Ag NP–rGO and other rGO-based materials previously reported, the Ag NTP–rGO pattern displays a low sheet resistance of 170 Ω $\square^{-1}$ with a transmittance of 90.2%. This inkjet-printed and reduction process can be broadened to obtain other metal–graphene patterns and devices.

Introduction

Inkjet-printing-based fabrication has been a promising approach with the rapid development and deployment of new material inks.[1–3] This technology has advantages including digitization, additive manufacturing, reduction of material waste, and compatibility with a variety of substrates. Various technologically important active components have been inkjet-printed,[4] including conducting electrodes,[5,6] transistors,[7,8] solar cells,[9] light-emitting diodes,[10] batteries,[11] and sensors.[12] However, the exploitation of patterning low-resistance electrodes with high light transmittance remains an important challenge. Although various metallic materials have been processed in solution to serve as electrodes, their inks are not stable in environmentally friendly solvents, such as water, which usually need organic addition agents,[4,13] and the high annealing temperature, high prices of the raw materials and the low conductivity of the electrodes limit their further applications.[14–17]

Graphene is a prominent contender as a metallic component in transparent electronic devices due to its high conductivity, chemical stability, and high transparency.[18–22] Various approaches are applied to the production of graphene. These encompass growth by chemical vapor deposition (CVD),[23–25] sublimation of Si atoms *via* heat treatment of silicon carbide,[26] and liquid phase exfoliation (LPE).[6,27] Among these, LPE offers significant advantages such as inexpensive raw materials, the potential for scalability, low thermal budget, which is ideally suited to produce printable inks. Previous studies have demonstrated inkjet printing of reduced graphene oxide (rGO) or pristine graphene flakes produced by the LPE method for organic thin-film transistor electrodes,[17] temperature sensors,[28] radio frequency applications,[29] chemical sensors,[12] and electronic devices. Nevertheless, because the size of graphene needs to be limited in a safe range <1/20 of that of a small nozzle, the electrical properties of inkjet-printed LPE-synthesized graphene are unsatisfactory (sheet resistance ~30 kΩ $\square^{-1}$).[6] Recently, some researchers combined CVD-formed graphene with metal materials, such as Ag or Au nanoparticles, to improve the conductivity.[30,31] Moreover, a conductive rGO/Ag hybrid electrode can be formed by depositing Ag on GO nanosheets and then reducing the GO.[32] However, due to the weak bonding between Ag and graphene,[33] it is difficult to obtain a homogeneous Ag–graphene hybrid ink, and the mechanism of the effect of the metal structure on the improved conductivity of metal–graphene is unclear. Therefore, it is still a challenge to inkjet-print conductive patterns with a metal and graphene-based

Key Laboratory of Green Printing, Institute of Chemistry, Chinese Academy of Sciences, Beijing, China. E-mail: ylsong@iccas.ac.cn; Fax: +86 6252 9284; Tel: +86 6252 9284

† Electronic supplementary information (ESI) available: Synthesis of Ag nanotriangle platelets and Ag polyhedral nanoparticles; the morphology and structure characterization of the as-synthesized samples *via* SEM, TEM, XRD and XPS; morphology of the inkjet-printed rGO-based patterns on glass substrates; and the analysis of C1s peak positions and the relative percentages of different C species with respect to GO, rGO, Ag NP–rGO, and Ag NTP–rGO. See DOI: 10.1039/c4ta04156a

hybrid ink, and to explore the structure effect of metal nanoparticles on the conductivity of graphene-based transparent patterns.

Graphene oxide (GO) nanosheets contain active groups that allow a variety of inorganic nanomaterials to be deposited on their surface.[32] Herein, we present a holistic approach to achieve high-performance printed Ag nanotriangle platelet–rGO (Ag NTP–rGO) and Ag polyhedral nanoparticle–rGO (Ag NP–rGO) patterns that addresses the entire process starting from graphene oxide exfoliation, ink formation, printing, to final reduction. Central to this approach is that the solvent of inks is only water, and monodisperse Ag nanotriangle platelets (Ag NTPs) and Ag polyhedral nanoparticles (Ag NPs) can be self-assembled on GO which is also used as a dispersant and a stabilizer, and after reduction, compared with rGO, Ag NP–rGO and other rGO-based materials previously reported, the Ag NTP–rGO pattern displays a low sheet resistance of 170 $\Omega\ \square^{-1}$ with a transmittance of 90.2%.

Experimental section

Materials

Graphite powder (99.998%, 200 mesh), silver nitrate ($AgNO_3$), L-ascorbic acid (AC), and trisodium citrate dihydrate (TCD) were purchased from Alfa Aesar. Sulfuric acid (>98%), potassium permanganate, hydrogen peroxide (H_2O_2, 30 wt%) and sodium borohydride ($NaBH_4$) were purchased from Beijing Chemical Reagents, P.R. China. All chemicals were used as received without further purification.

Materials preparation

Synthesis of graphene oxide (GO) sheets. The GO nanosheet was synthesized according to a reported method.[34] The graphite powder (3 g) was added into concentrated H_2SO_4 (120 mL). Then $KMnO_4$ (15 g) was added gradually while stirring, and the temperature of the mixture was kept below 20 °C for 2 h using an ice bath. Successively, the mixture was stirred at 38 °C for 2 h and diluted with deionized water (500 mL) to maintain the temperature at 50 °C. Additional water (420 mL) and 30% H_2O_2 (20 mL) were added, producing a brilliant yellow mixture. The mixture was filtered and washed with a 10% HCl aqueous solution to remove metal ions, which was followed by a deionized water wash to remove the acid. Then the as-prepared GO was treated by using an ultrasonic homogenizer (4710 series, Cole Parmer Instrument Co.) under 200 W for 2 h and was passed through a 0.8 μm filter to remove large sized GO. The solid obtained on the filter was vacuum dried overnight at room temperature.

Synthesis of Ag nanoplates (Ag NTPs). Triangular Ag nanoplates with controlled size and thickness were synthesized by a modified chemical reduction method reported by Mirkin *et al.*[35] and a seeded deposition method developed by Yin and Xia *et al.*[36,37] A typical synthesis is described in the ESI.† To control the size of Ag NTPs, it is needed to carefully regulate the reaction time, reactant concentration, and the rate of the reactant addition.

Synthesis of Ag nanoparticles (Ag NPs). The monodisperse Ag nanoparticles were synthesized in water according to ref. 38. A typical synthesis is also described in the ESI.† Especially, KI was added at low temperature (<80 °C) to obtain Ag polyhedral nanoparticles (about 70 nm).

Ink preparation

Preparation of inks for printing (ink of GO, Ag nanoplate–GO (Ag NTP–GO) and Ag nanoparticle–GO (Ag NP–GO)). To form the ink of GO, the as-prepared GO was dispersed in deionized (DI) water at a concentration of 2.4 wt% by bath sonication. The resulting ink was passed through a 0.8 μm filter to remove any dust or contaminant that could destabilize printing. To form the ink of Ag NTP–GO (or Ag NP–GO), the Ag NTPs (or Ag NPs) were assembled on the GO surface as follows: 3 mg of the Ag NTPs (or Ag NPs) dispersed in 20 mL of water was added into 20 mL of GO aqueous solution ink (1.5 mg mL^{-1}), and the mixture was treated by ultrasonication for 1 h. Then, the as-prepared Ag NTP–GO (or Ag NP–GO) ink was treated by the same process as that used for the GO ink, which was dispersed in deionized (DI) water at a concentration of 2.4 wt% by bath sonication and then passed through the filter. The viscosity of the inks was 13.0 mPa S for GO, 13.7 mPa S for Ag NTP–GO and 13.9 mPa S for Ag NP–GO. The surface tension of the inks was 52.3 mN m^{-1} for GO, 50.2 mN m^{-1} for Ag NTP–GO and 49.4 mPa S for Ag NP–GO.

Printing

The prepared ink was injected into a cartridge for use and printed by using a Dimatix Materials Printer (FUJIFILMDMP-2800 series, Japan) with a 10 pL drop cartridge (DMC-11610). The printing was carried out at 30 °C. The glass wafers were used as substrates, which were cleaned by bath sonication in water for 20 minutes followed by drying under a stream of N_2. The resulting water contact angle was ~14° for GO, ~12.2° for Ag NTP–GO and 10.1° for Ag NP–GO.

Reduction

The inkjet-printed samples were placed into a vacuum drying oven, and 1 mL of aqueous hydrazine monohydrate in a small beaker was added. They were vacuumized to about 10 Pa by using a mechanical pump and then heated at 110 °C for 3 h.

Characterization

The viscosity of the inks was measured by using a viscometer (SV-10, A&D Company Limited, Japan) at 30 °C, and the surface tension of the inks was characterized by using a full automatic surface tension meter (K100SF, KRÜSS GmbH Germany). The transmission electron microscopy (TEM) images were taken with a JEOL JEM-1011 transmission electron microscope operating at 100 kV. The size and structure of silver nanoparticles were characterized by using a JEOL JEM-2100F transmission electron microscope operating at 200 kV, and the samples were prepared by dropwise addition of the solution onto a carbon-coated copper grid. The scanning electron microscopy (SEM) images were taken with an S-4800 (Japan Hitachi) transmission

electron microscope. The transparency spectra were measured with a UV visible spectrophotometer (UV-2600, Japan Shimadzu). The structures of the patterns were investigated by using an optical microscope with a high speed CCD (MX40, Japan Olympus). X-ray photoelectron spectroscopy (XPS) was performed on a Thermo Scientific ESCALab 250Xi using 200 W monochromated Al Kα radiation. The 500 μm X-ray spot was used for XPS analysis. The sheet resistance and the current–voltage curve of the resulting patterns were measured by using a 4-point probe nanovoltmeter (model: AS-3505C, Kasaha Laboratory Ltd., Japan).

Results and discussion

The formation process of the rGO/Ag hybrid is illustrated in Fig. 1. To prepare the rGO/Ag hybrid, the GO suspension was first mixed with as-synthesized polyhedral or platelet-like Ag nanoparticles (the details of synthesis of Ag are described in the ESI†), respectively, the GO-based ink was then inkjet-printed, and finally the inkjet-printed patterns were reduced in hydrazine vapor at 110 °C for further characterization and measurements.

As evidence of the different Ag particles by the TEM and SEM images shown in Fig. 2a, c, and S1 (see ESI†), the as-obtained Ag nanoparticles (Ag NPs) are monodisperse polyhedral nanoparticles with 70 nm in diameter and Ag nanotriangle platelets (Ag NTPs) with the length of the perpendicular bisector also being about 70 nm. To understand the structures of the composite, HRTEM analysis of Ag NTPs is performed (Fig. 2e and f). The flat exposed crystal facets are {111}, corresponding to the lattice spacing of 1.44 Å, indexed to the {220} of face-centered cubic (fcc) Ag (JCPDS card number: 04-0783). Due to citrate selectively binding to Ag (111), it favors to form Ag enclosed preferentially by {111} facets. From the high resolution fast Fourier transform diffraction pattern of Ag NTPs, it is found that the six bright spots with 6-fold symmetry can be indexed to the {220} reflections of the fcc crystal oriented in the [111] direction, and the appearance of strong diffraction spots of 1/3 {422} reflections is normally forbidden for fcc Ag lattices, indicating the existence of multiple {111} twin planes parallel to the basal surfaces of the nanoplates.[39–41] The TEM images of the as-prepared Ag NP–GO and Ag NTP–GO are shown in Fig. 2b, d, and S1,† and their homogeneous inks (the inset in Fig. 2b and d) are obtained by simply adding them in water, in which GO can be used as a dispersant and a stabilizer. It was found that mixing the Ag NPs or Ag NTPs with GO sheets under sonication in water led to direct self-assembly of a layer of Ag on GO, which was similar to that observed by Sun,[42] and the Ag NTPs lay flat on the GO and the edge of the Ag nanoplatelets became round.

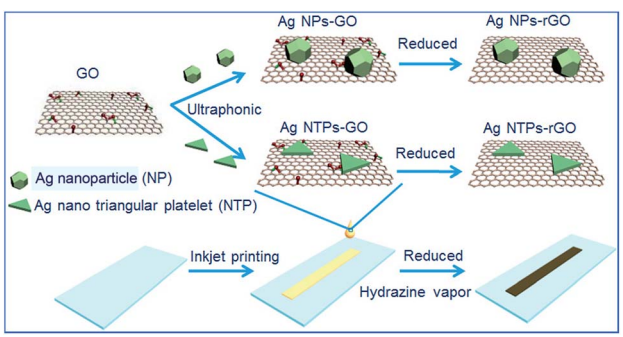

Fig. 1 Schematic illustration of the inkjet-printed pattern preparation processes.

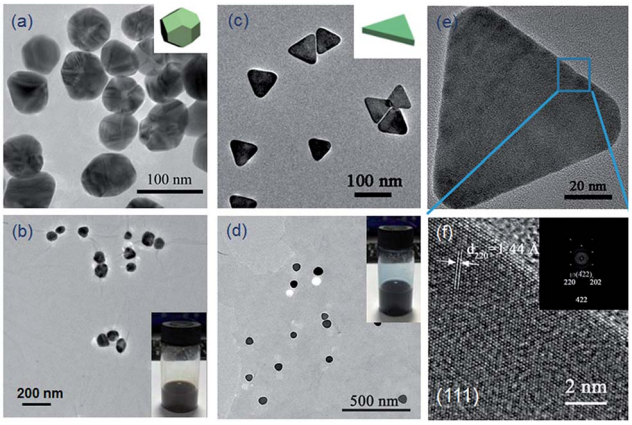

Fig. 2 The TEM images of the as-synthesized (a) Ag NPs, (b) Ag NP–GO (the inset is the photograph of the Ag NP–GO ink), (c) Ag NTPs, (d) Ag NTP–GO (the inset is the photograph of the Ag NTP–GO ink) and the HRTEM image of the as-synthesized (e and f) Ag NTPs, and the inset is a high resolution fast Fourier transform diffraction pattern of Ag NTPs.

The inkjet printing was carried out at 30 °C using a Fujifilm Dimatix Materials Printer (DMP 2800) with a cartridge designed for a 10 pL nominal drop volume. Drop spacing for all printed features was maintained at 33 μm. The inkjet-printed samples were then reduced. To analysis the structure of the rGO-based samples, the XRD measurements were carried out (ESI, Fig. S2†). It is shown that, after reduction, the inter-planar distance of the rGO is decreased to 3.69 Å (24.6°) from 8.60 Å (10.3°) for the original GO, due to the decrease of the oxygen-containing groups on the graphene (G) sheets. Exactly as shown in the ESI, Fig. S2c,† the peaks of Ag NP–rGO at 38.1° and 44.3° are characteristic of face-centered cubic crystalline Ag, corresponding to the planes (111) and (200) (JCPDS card number: 04-0783). It is interesting to find that only a peak at around 38.1° can be observed from the XRD pattern of Ag NP–rGO, which can be assigned to the {111} plane refection of Ag (JCPDS card number: 04-0783), and the peak at around 44.3° almost cannot be found (see ESI, Fig. S2d†). It indicates that the surface planes of the product are aligned unidirectionally, normal to the {111} face on the rGO sheets. It is in agreement with the results of TEM and HRTEM (Fig. 2d and f), from which the Ag NTPs lying flat on the GO sheets with {111} face can be observed.

To further elucidate the reduction process, high resolution C1s peaks in the X-ray photoelectron spectra (XPS) of the GO, rGO, Ag NP–rGO, and Ag NTP–rGO are obtained (Fig. S3 (ESI†) and Fig. 3a–c). The deconvolution of the bands shows that the peaks at the binding energy of 284.8 eV are attributed to the C–C, C=C, and C–H bonds, and the peaks centered at the

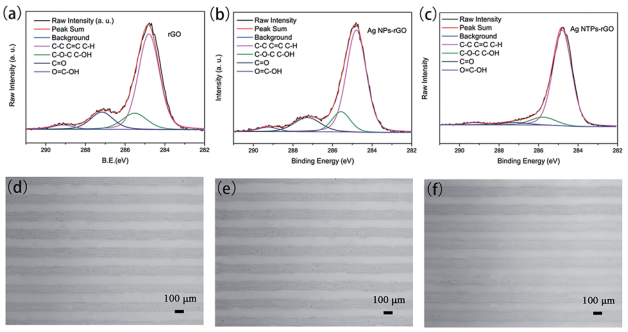

Fig. 3 The XPS spectra of C1s peaks of as-synthesized (a) rGO, (b) Ag NP–rGO, and (c) Ag NTP–rGO. Morphology of the inkjet-printed rGO-based patterns on glass substrates. Optical microscopy images of the printed lines of (d) rGO (e) Ag NP–rGO and (f) Ag NTP–rGO illustrate the uniformity of the printed features.

binding energies of 285.5–285.8 eV, 287.2–287.3 eV, and 288.9–289.2 eV are assigned to the C–OH, C=O, and O=C–OH oxygen-containing carbonaceous bands, respectively, as described previously.[43] The detailed analysis of the C1s peak positions and the relative percentages of different C species are listed in the ESI, Table S1.† The percentage of C–C, C=C, and C–H bonds in the order of Ag NTP–rGO > Ag NP–rGO > rGO > GO indicates that the reduction degree of rGO species is in the order of Ag NTP–rGO > Ag NP–rGO > rGO.

From the optical microscopy images, the patterns show no undesirable coffee ring effects, and the width of the inkjet-printed rGO-based lines on glass is about 100 μm (Fig. 3d–f, and S4 (ESI†)). The fine morphology of the inkjet-printed patterns is due to the suppression of the coffee ring effect *via* a Marangoni flow established by the surface tension gradient.[4,44,45] This flow homogenizes the droplet composition, resulting in a uniform morphology of the printed features. Furthermore, the sp^2 bonding, oxygen functional groups and small lateral size of the GO flakes minimize folding or buckling of the inkjet-printed flakes, which promotes low surface roughness and well-defined flake–flake contacts.

Fig. 4 shows the optical properties of inkjet-printed rGO-based patterns ($1 \times 1\ cm^2$) on glass. The transmittance data as a function of wavelength for the corresponding rGO-based inkjet-printed patterns are shown in Fig. 4b with the inset of their voltage–current (*IV*) curves ranging from −4 V to 4 V. Amount them, the transparency at the same wavelength is in the order of rGO > Ag NTP–rGO > Ag NP–rGO with the transmittance (93%, 90% and 87%) at a wavelength of 550 nm, respectively, which is enough for most transparent conducting electrode-based applications.[46] Though the addition of Ag NTPs and Ag NPs reduces the optical transmittance of Ag NTP–rGO and Ag NP–rGO, the transparency of Ag NTP–rGO is higher than that of Ag NP–rGO due to the thin thickness of Ag NTPs.

To study the electrical properties of the as-prepared rGO-based patterns, different inkjet-printed layers of patterns were obtained. It is found that their sheet resistivity (R_s) reaches a relatively low value. Fig. 5, S5 and S6 (ESI†) show sheet resistances and optical transmittances of the inkjet-printed rGO-based patterns compared to other transparent graphene-based

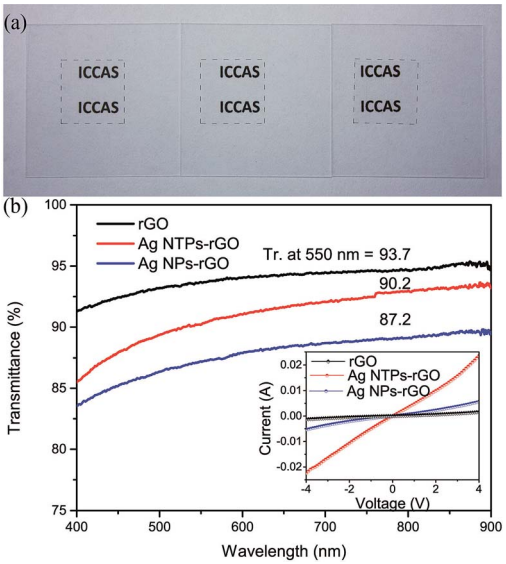

Fig. 4 (a) The transparent rGO (left), Ag NTP–rGO (middle), and Ag NP–rGO (right) patterns ($1 \times 1\ cm^2$) inkjet-printed on glass substrates. Analysis and comparison of transparent patterns: (b) transparency spectra of one inkjet-printed layer of rGO, Ag NP–rGO, and Ag NTP–rGO inkjet-printed patterns on glass substrates. The inset shows the voltage–current *IV* curve of rGO, Ag NP–rGO, and Ag NTP–rGO ranging from −4 V to 4 V. The transparency (Tr.) was defined as the transmittance at a wavelength of 550 nm.

(including LPE-synthesized G and CVD-growth G) films from previous research results. The as-prepared rGO, Ag NTP–rGO and Ag NP–rGO patterns have $R_s = 2.5\ k\Omega\ \square^{-1}$ ($T_{550} = 93\%$), $R_s = 170\ \Omega\ \square^{-1}$ ($T_{550} = 90\%$) and $R_s = 639\ \Omega\ \square^{-1}$ ($T_{550} = 87\%$), respectively, and the value of sheet resistance of rGO species is in the order of Ag NTP–rGO < Ag NP–rGO < rGO, which is in agreement with the reduction degree of rGO species indicated in the XPS measurement (Fig. 3). This confirms that the R_s of the rGO-based patterns is affected by the oxygen functional groups. It is found that the obtained Ag NTP–rGO pattern with good

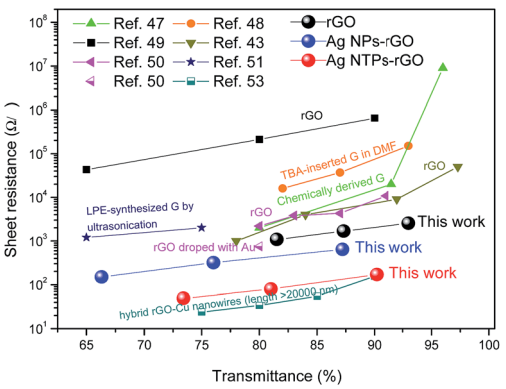

Fig. 5 Sheet resistance *vs.* transmittance of inkjet-printed rGO-based electrodes which corresponds to one inkjet-printed layer, two inkjet-printed layers and three inkjet-printed layers with a downward trend of the transmittance, compared to other transparent LPE-synthesized G-based electrodes from previous research results.

transparency (90%) shows a lower sheet resistance value (R_s = 170 Ω □$^{-1}$) than that of LPE-synthesized G films with similar transparency reported in the literature (Fig. 5).[43,47–51] The R_s of the Ag NTP–rGO pattern is also lower than that of Au-doped rGO and CVD-growth G (Fig. S5 (ESI†)),[20,52] reaches the value of that of hybrid rGO–Cu nanowires (length > 20 μm, too long to be suitable for inkjet printing),[53] and is close to that of hydrazine-doped CVD-growth G[54] and CVD-growth G/Ag nanowires (Fig. S5 (ESI†)).[30,55]

The reasons of conductivity enhancement of Ag–rGO can be explained as follows: when the GO and Ag nanoparticles (Ag NTPs, Ag NPs) are mixed, the oxygen-containing functional groups of GO come into contact with the silver nanoparticles. Then when the GO is reduced, the oxygen-containing functional groups are removed, the distance between silver and rGO decreases (see Fig. 6), the d orbitals of Ag interact with the π orbitals of rGO, and the conductivity of Ag nanoparticle–rGO is improved. A similar phenomenon is observed for the Cu nanowire–rGO hybrid in a previous report.[53] Especially, Ag nanoplates further enhance the conductivity of Ag NTP–rGO. On one hand, rGO–Ag–rGO forms a sandwich structure, more contact area between Ag and rGO is formed in Ag NTP–rGO than Ag NP–rGO (see Fig. 6 and S7 (ESI†)), the {111} plane of Ag nanoplatelets is the low energy face, and the theoretical distance (0.33 nm) between the Ag {111} plane and the graphene {001} plane is smaller than that between polyhedral Ag and graphene {001} planes,[33] which can make the electron transport between Ag and graphene easy, resulting in enhanced conductivity of the Ag NTP–rGO composite. On the other hand, the binding of Ag to rGO is important for the conductivity of the rGO-based patterns. Ag 3d XPS spectra are used to analyze the binding between Ag and reduced graphene oxide of the Ag NTP–rGO and Ag NP–rGO, as shown in Fig. 7. Since the work function of Ag (4.2 eV) is smaller than that of graphene (4.8 eV),[56] electron transfer from the Ag to graphene sheets can occur during the formation of the Ag–rGO heterostructures. The Ag 3d peaks

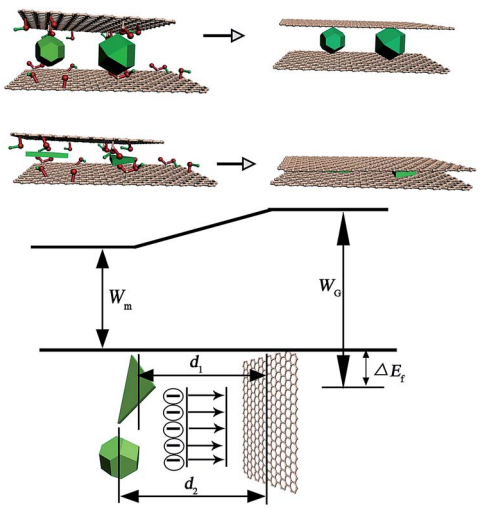

Fig. 6 Illustration of the energy diagram and transportation of electrons at the graphene–metal interface.

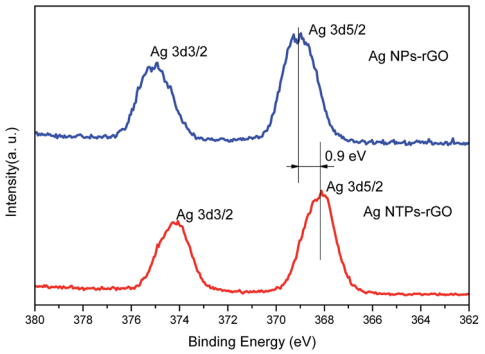

Fig. 7 The XPS patterns of Ag peaks of the as-synthesized Ag NP–rGO and Ag NTP–rGO.

shift nearly 0.9 eV to lower binding energies at 368.2 eV and 374.3 eV for Ag NTP–rGO compared with 369.1 eV and 375.2 eV for Ag NP–rGO, due to more electron transfer from Ag NTPs than that from Ag NPs to the rGO sheet, and the smaller distance between Ag NTPs and the rGO sheet than that between Ag NPs and the rGO sheet. Thus the conductivity of Ag NTP–rGO is highly improved.

Conclusions

A holistic approach for achieving highly conductive inkjet-printed Ag NTP–rGO hybrid transparent patterns is demonstrated. Monodisperse Ag NTPs can be self-assembled on GO, and the low-energy {111} facet of Ag NTPs is oriented on GO {001} facets. In this system, GO is also used as a dispersant and a stabilizer, and water is used as a solvent to prepare inks for inkjet printing. After reduction, the printed Ag NTP–rGO pattern shows a low sheet resistance of 170 Ω □$^{-1}$ with a high transmittance of 90.2%. This inkjet-printed and reduction process can be broadened to obtain other metal–graphene patterns, and will be of significance for the development of metal–graphene based functional devices.

Acknowledgements

The authors gratefully acknowledge financial support from the National Key Scientific Program (grant number 2013CB933004), the NSFC (grant numbers 21301180, 51173190, 21121001, 21203209 and 51473172), the "Strategic Priority Research Program" of the Chinese Academy of Sciences (grant number XDA09020000), and the National High Technology Research and Development Program of China (Grant no. 2013AA030802).

Notes and references

1 B. Y. Ahn, E. B. Duoss, M. J. Motala, X. Guo, S.-I. Park, Y. Xiong, J. Yoon, R. G. Nuzzo, J. A. Rogers and J. A. Lewis, *Science*, 2009, **323**, 1590–1593.
2 M. Kuang, L. Wang and Y. Song, *Adv. Mater.*, 2014, DOI: 10.1002/adma.201305416.

3 Z. Zhang, X. Zhang, Z. Xin, M. Deng, Y. Wen and Y. Song, *Adv. Mater.*, 2013, **25**, 6714–6718.
4 M. Singh, H. M. Haverinen, P. Dhagat and G. E. Jabbour, *Adv. Mater.*, 2010, **22**, 673–685.
5 E. B. Secor, P. L. Prabhumirashi, K. Puntambekar, M. L. Geier and M. C. Hersam, *J. Phys. Chem. Lett.*, 2013, **4**, 1347–1351.
6 F. Torrisi, T. Hasan, W. Wu, Z. Sun, A. Lombardo, T. S. Kulmala, G.-W. Hsieh, S. Jung, F. Bonaccorso, P. J. Paul, D. Chu and A. C. Ferrari, *ACS Nano*, 2012, **6**, 2992–3006.
7 H. Yan, Z. Chen, Y. Zheng, C. Newman, J. R. Quinn, F. Dotz, M. Kastler and A. Facchetti, *Nature*, 2009, **457**, 679–686.
8 J. W. Hennek, Y. Xia, K. Everaerts, M. C. Hersam, A. Facchetti and T. J. Marks, *ACS Appl. Mater. Interfaces*, 2012, **4**, 1614–1619.
9 E. Martinez-Ferrero, I. Burgues-Ceballos, M. Stella and P. Lacharmoise, *J. Mater. Chem. A*, 2014, **2**, 17711–17722.
10 V. Wood, M. J. Panzer, J. Chen, M. S. Bradley, J. E. Halpert, M. G. Bawendi and V. Bulović, *Adv. Mater.*, 2009, **21**, 2151–2155.
11 K. Sun, T.-S. Wei, B. Y. Ahn, J. Y. Seo, S. J. Dillon and J. A. Lewis, *Adv. Mater.*, 2013, **25**, 4539–4543.
12 V. Dua, S. P. Surwade, S. Ammu, S. R. Agnihotra, S. Jain, K. E. Roberts, S. Park, R. S. Ruoff and S. K. Manohar, *Angew. Chem., Int. Ed.*, 2010, **49**, 2154–2157.
13 N. A. Luechinger, E. K. Athanassiou and W. J. Stark, *Nanotechnology*, 2008, **19**, 445201.
14 H. Sirringhaus, T. Kawase, R. H. Friend, T. Shimoda, M. Inbasekaran, W. Wu and E. P. Woo, *Science*, 2000, **290**, 2123–2126.
15 Y. Zhao, C.-a. Di, X. Gao, Y. Hu, Y. Guo, L. Zhang, Y. Liu, J. Wang, W. Hu and D. Zhu, *Adv. Mater.*, 2011, **23**, 2448–2453.
16 L. Zhang, H. Liu, Y. Zhao, X. Sun, Y. Wen, Y. Guo, X. Gao, C.-a. Di, G. Yu and Y. Liu, *Adv. Mater.*, 2012, **24**, 436–440.
17 S. Lim, B. Kang, D. Kwak, W. H. Lee, J. A. Lim and K. Cho, *J. Phys. Chem. C*, 2012, **116**, 7520–7525.
18 R. R. Nair, P. Blake, A. N. Grigorenko, K. S. Novoselov, T. J. Booth, T. Stauber, N. M. R. Peres and A. K. Geim, *Science*, 2008, **320**, 1308.
19 W. Yuan and G. Shi, *J. Mater. Chem. A*, 2013, **1**, 10078–10091.
20 K. S. Kim, Y. Zhao, H. Jang, S. Y. Lee, J. M. Kim, K. S. Kim, J.-H. Ahn, P. Kim, J.-Y. Choi and B. H. Hong, *Nature*, 2009, **457**, 706–710.
21 J. U. Park, S. Nam, M. S. Lee and C. M. Lieber, *Nat. Mater.*, 2012, **11**, 120–125.
22 S. J. Guo, S. Zhang and S. H. Sun, *Angew. Chem., Int. Ed.*, 2013, **52**, 8526–8544.
23 X. Li, W. Cai, J. An, S. Kim, J. Nah, D. Yang, R. Piner, A. Velamakanni, I. Jung, E. Tutuc, S. K. Banerjee, L. Colombo and R. S. Ruoff, *Science*, 2009, **324**, 1312–1314.
24 K. S. Novoselov, V. I. Falko, L. Colombo, P. R. Gellert, M. G. Schwab and K. Kim, *Nature*, 2012, **490**, 192–200.
25 W. J. Fang, A. L. Hsu, Y. Song, A. G. Birdwell, M. Amani, M. Dubey, M. S. Dresselhaus, T. Palacios and J. Kong, *ACS Nano*, 2014, **8**, 6491–6499.
26 Y.-M. Lin, C. Dimitrakopoulos, K. A. Jenkins, D. B. Farmer, H.-Y. Chiu, A. Grill and P. Avouris, *Science*, 2010, **327**, 662.
27 W. S. Hummers and R. E. Offeman, *J. Am. Chem. Soc.*, 1958, **80**, 1339.
28 D. Kong, L. T. Le, Y. Li, J. L. Zunino and W. Lee, *Langmuir*, 2012, **28**, 13467–13472.
29 K.-Y. Shin, J.-Y. Hong and J. Jang, *Adv. Mater.*, 2011, **23**, 2113–2118.
30 I. N. Kholmanov, C. W. Magnuson, A. E. Aliev, H. Li, B. Zhang, J. W. Suk, L. L. Zhang, E. Peng, S. H. Mousavi, A. B. Khanikaev, R. Piner, G. Shvets and R. S. Ruoff, *Nano Lett.*, 2012, **12**, 5679–5683.
31 K. K. Kim, A. Reina, Y. Shi, H. Park, L.-J. Li, Y. H. Lee and J. Kong, *Nanotechnology*, 2010, **21**, 285205.
32 L. Lu, J. Liu, Y. Hu, Y. Zhang and W. Chen, *Adv. Mater.*, 2013, **25**, 1270–1274.
33 G. Giovannetti, P. A. Khomyakov, G. Brocks, V. M. Karpan, J. van den Brink and P. J. Kelly, *Phys. Rev. Lett.*, 2008, **101**, 026803.
34 L. H. Li, Y. e. Wu, J. Lu, C. Y. Nan and Y. D. Li, *Chem. Commun.*, 2013, **49**, 7486–7488.
35 G. S. Métraux and C. A. Mirkin, *Adv. Mater.*, 2005, **17**, 412–415.
36 Q. Zhang, Y. Hu, S. Guo, J. Goebl and Y. Yin, *Nano Lett.*, 2010, **10**, 5037–5042.
37 J. Zeng, X. Xia, M. Rycenga, P. Henneghan, Q. Li and Y. Xia, *Angew. Chem., Int. Ed.*, 2011, **50**, 244–249.
38 H. Li, H. Xia, D. Wang and X. Tao, *Langmuir*, 2013, **29**, 5074–5079.
39 R. Jin, Y. Charles Cao, E. Hao, G. S. Metraux, G. C. Schatz and C. A. Mirkin, *Nature*, 2003, **425**, 487–490.
40 D. Aherne, D. M. Ledwith, M. Gara and J. M. Kelly, *Adv. Funct. Mater.*, 2008, **18**, 2005–2016.
41 Q. Zhang, N. Li, J. Goebl, Z. Lu and Y. Yin, *J. Am. Chem. Soc.*, 2011, **133**, 18931–18939.
42 S. Guo and S. Sun, *J. Am. Chem. Soc.*, 2012, **134**, 2492–2495.
43 H. A. Becerril, J. Mao, Z. Liu, R. M. Stoltenberg, Z. Bao and Y. Chen, *ACS Nano*, 2008, **2**, 463–470.
44 H. Masoud and H. A. Stone, *J. Fluid Mech.*, 2014, 741.
45 J. A. Lim, W. H. Lee, H. S. Lee, J. H. Lee, Y. D. Park and K. Cho, *Adv. Funct. Mater.*, 2008, **18**, 229–234.
46 Y. Zhu, Z. Sun, Z. Yan, Z. Jin and J. M. Tour, *ACS Nano*, 2011, **5**, 6472–6479.
47 H. Yamaguchi, G. Eda, C. Mattevi, H. Kim and M. Chhowalla, *ACS Nano*, 2010, **4**, 524–528.
48 X. Li, G. Zhang, X. Bai, X. Sun, X. Wang, E. Wang and H. Dai, *Nat. Nanotechnol.*, 2008, **3**, 538–542.
49 G. Eda, G. Fanchini and M. Chhowalla, *Nat. Nanotechnol.*, 2008, **3**, 270–274.
50 S. Y. Jeong, S. H. Kim, J. T. Han, H. J. Jeong, S. Yang and G.-W. Lee, *ACS Nano*, 2011, **5**, 870–878.
51 A. A. Green and M. C. Hersam, *Nano Lett.*, 2009, **9**, 4031–4036.
52 X. Li, Y. Zhu, W. Cai, M. Borysiak, B. Han, D. Chen, R. D. Piner, L. Colombo and R. S. Ruoff, *Nano Lett.*, 2009, **9**, 4359–4363.

53 I. N. Kholmanov, S. H. Domingues, H. Chou, X. Wang, C. Tan, J.-Y. Kim, H. Li, R. Piner, A. J. G. Zarbin and R. S. Ruoff, *ACS Nano*, 2013, **7**, 1811–1816.
54 J. B. Bult, R. Crisp, C. L. Perkins and J. L. Blackburn, *ACS Nano*, 2013, **7**, 7251–7261.
55 M.-S. Lee, K. Lee, S.-Y. Kim, H. Lee, J. Park, K.-H. Choi, H.-K. Kim, D.-G. Kim, D.-Y. Lee, S. Nam and J.-U. Park, *Nano Lett.*, 2013, **13**, 2814–2821.
56 T. Wu, H. Shen, L. Sun, B. Cheng, B. Liu and J. Shen, *ACS Appl. Mater. Interfaces*, 2012, **4**, 2041–2047.